

In Situ Time-Resolved Studies of Octacalcium Phosphate and Dicalcium Phosphate Dihydrate in Simulated Body Fluid: Cooperative Interactions and Nanoapatite Crystal Growth

Julietta V. Rau,^{*,†} Marco Fosca,^{†,‡} Vladimir S. Komlev,[§] Inna V. Fadeeva,[§]
Valerio Rossi Albertini,[†] and Sergey M. Barinov[§]

[†]Istituto di Struttura della Materia, Consiglio Nazionale delle Ricerche, Via del Fosso del Cavaliere, 100 - 00133 Rome, Italy, [‡]Dipartimento di Chimica, "Sapienza" Università di Roma, Piazzale Aldo Moro, 5-00185 Rome, Italy, and [§]A. A. Baikov Institute of Metallurgy and Materials Science, Russian Academy of Sciences, Leninsky prospect 49, 119991 Moscow, Russia

Received June 4, 2010; Revised Manuscript Received June 18, 2010

ABSTRACT: The present study is focused on the in vitro study of the biphasic octacalcium phosphate (OCP)–dicalcium phosphate dihydrate (DCPD) system transformations in simulated body fluid (SBF) for possible applications as bone substitute materials. The aim of this paper is to outline the role of the additional component DCPD during a transformation/crystallization processes. Energy dispersive X-ray diffraction and FTIR spectroscopy techniques were used for in situ monitoring of the processes taking place in the system in real time. Morphological investigations were performed applying the scanning electron microscopy technique. Several OCP–DCPD combinations were investigated: (1) 100% OCP; (2) 70% OCP–30% DCPD; (3) 100% DCPD. The obtained experimental results allowed us to conclude that when only OCP is present in SBF, the formation of carbonated hydroxyapatite takes place, whereas for the OCP–DCPD (30%) system in SBF, less kinetically favorable hydroxyapatite (HA) is formed. The additional component (DCPD) influences significantly the structural behavior of hydroxyapatite, acting as the HA crystallization inhibition agent. By means of this approach, allowing for the control of the HA crystallization, the calcium phosphate based biomaterials can be suitably modified for implant use in bone tissue engineering. The results obtained in this work provided some insights into the biomineralization mechanism.

1. Introduction

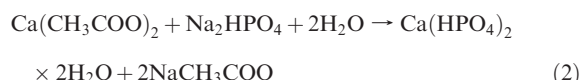
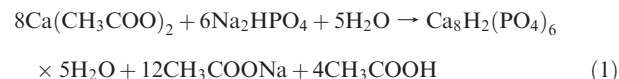
A number of calcium phosphate materials based on hydroxyapatite (HA, $\text{Ca}_{10}(\text{PO}_4)_6(\text{OH})_2$) are widely used as biomaterials, and, particularly, as scaffolds for bone tissue engineering.^{1–3} Among them, octacalcium phosphate (OCP, $\text{Ca}_8\text{H}_2(\text{PO}_4)_6 \cdot 5\text{H}_2\text{O}$) is considered to be of particular interest,^{4–7} since it has been reported to be a direct precursor phase during the biomineralization process of bones and teeth.^{8–10} The biocompatibility and the osteoconductive nature of synthetic OCP are widely acknowledged.^{11,12} Furthermore, recent studies have shown that OCP enhances a new bone formation, accompanied by its conversion into hydroxyapatite products and its own biodegradation by the osteoclast cells activities.^{13–15}

However, the nature of the precursor phase during the biomineralization process is still controversial,^{16–18} several phases being hypothesized. They include, along with octacalcium phosphate, dicalcium phosphate dihydrate (DCPD, $\text{CaHPO}_4 \cdot 2\text{H}_2\text{O}$, brushite).^{19,20} Several studies^{20–23} suggested that OCP is the direct precursor phase of HA, since the results of in vitro (in simulated body fluid) crystal growth studies showed that DCPD can be hydrolyzed to HA via the OCP formation.²⁰ According to the literature data,^{20,24} the transformation of OCP into HA can proceed via either (1) in situ hydrolysis of apatitic layers or (2) de novo precipitation of apatite crystals on the OCP crystal templates, that is the process of OCP dissolution followed by the reprecipitation of apatite crystals.

To the best of our knowledge, this study is the first to report on the cooperative effect of the OCP–DCPD combination in SBF, resulting in HA formation. To study this effect, pure OCP and DCPD components and their combination were mixed with a SBF having ion concentrations close to those of human blood plasma, a condition that is very useful for predicting of the in vivo bone bioactivity of a material.^{25,26} The materials were analyzed both ex and in situ, applying the nonconventional energy dispersive X-ray diffraction technique (EDXRD) and the conventional Fourier transform infrared (FTIR) spectroscopy. Scanning electron microscopy (SEM) morphological studies were also carried out. A better understanding of pure OCP and DCPD transformations, and the effect of the additional DCPD phase presence during the hydrolysis, may lead not only to the development of new bone substitute materials, but also to the elucidation of the biomineralization mechanism of bone formation.

2. Experimental Section

Synthesis of Powders. Octacalcium phosphate (OCP), dicalcium phosphate dihydrate (DCPD, brushite), and OCP/DCPD biphasic system were obtained according to the wet precipitation method:



Chemically pure calcium acetate and sodium acid phosphate (Merck, Germany) were used to obtain OCP, DCPD, and their biphasic combination. Calcium acetate solution (0.04 mol/L, 250 mL) and sodium acid phosphate solution (0.04 mol/L, 250 mL) were

*Corresponding author. Phone: +39-06-4993-4086; fax: +39-06-4993-4153; e-mail: giulietta.rau@ism.cnr.it.

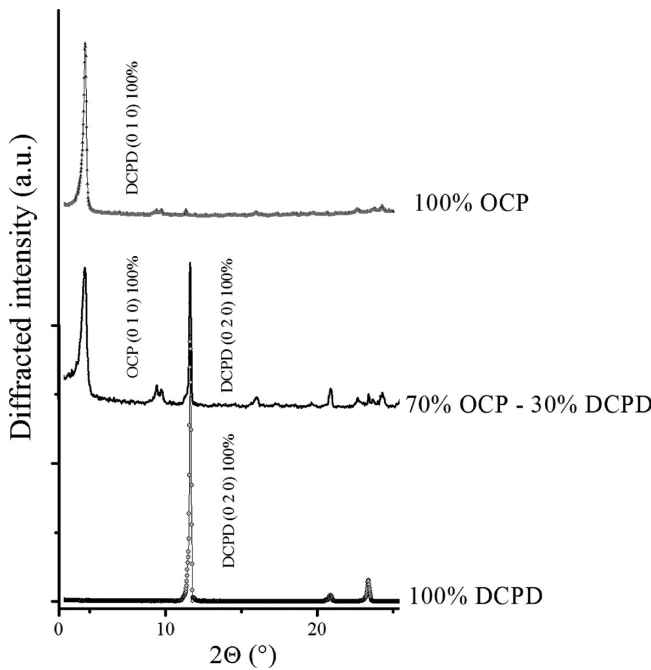


Figure 1. ADXRD patterns of the pristine samples: (top) 100% OCP; (middle) 70% OCP – 30% DCPD; (bottom) 100% DCPD.

Table 1. Phase Composition of the Investigated Systems

sample number	phase composition	
	OCP, wt %	DCPD (brushite), wt %
1	100	0
2	70	30
3	0	100

heated in the temperature range of 25–90 °C, and a solution with the pH in the range of 5.0–5.5 was obtained. The sodium phosphate solution was added drop-wise to the calcium acetate solution and stirred during the precipitation. After 1 h, the precipitates were filtered and dried at room temperature. Phase composition of the obtained substances was analyzed by a conventional X-ray diffraction technique (angular dispersive X-ray diffraction (ADXRD)) (“SHIMADZU-6000” (Japan) Ni-filtered Cu-target, $\lambda = 1.54183 \text{ \AA}$), and the results are reported in Figure 1 and Table 1.

The proportion component (X_a) of crystalline phases of OCP and DCPD in sample 2 was evaluated by the following equation:

$$X_a = I_{ia} / (RIR_a \times I^{rel,ia}) \times [\sum_k (I_{jk} / (RIR_j \times I^{rel,jk}))]^{-1} \quad (3)$$

where I_{ia} is the intensity of OCP (010) reflection; $I^{rel,ia}$ is relative intensity of OCP (010) reflection from JCPDS database; RIR_a - corundum number for OCP phase is 0.5; I_{jk} , $I^{rel,jk}$ and RIR_k corresponding values for all phases (OCP (010) reflection and DCPD (020) reflections were used). The corundum number for DCPD phase is 1.4.

To confirm the chemical composition of the samples, their infrared absorption spectra were collected by a Nicolet Avatar 330 FT-IR spectrometer in the 4000–400 cm⁻¹ range, the powders being pelleted in KBr.

SBF Preparation. For the in vitro investigation, a SBF with ion concentrations (Na⁺ 142.0, K⁺ 5.0, Ca²⁺ 2.5, Mg²⁺ 1.5, Cl⁻ 147.8, HCO₃⁻ 4.2, HPO₄²⁻ 1.0, SO₄²⁻ 0.5 mM) nearly equal to those of human blood plasma at 36.5 °C was prepared according to ref 27. The SBF was obtained by dissolving reagent-grade chemicals of NaCl, NaHCO₃, KCl, K₂PO₄·3H₂O, MgCl₂·6H₂O, CaCl₂, and Na₂SO₄ into distilled water, and buffered at pH 7.40 with tris-hydroxymethyl-aminomethane ((HOCH₂)₃CNH₂) (Tris) and 1 M hydrochloric acid at 36.5 °C.

Energy Dispersive X-ray Diffraction Characterization. The EDXRD measurements were executed by a noncommercial machine,²⁸ based

on the use of a W-anode tube (supplied at 55 kV), as a polychromatic (“white”) photon source, and of an ultrapure solid-state Ge photodiode, as an energy-sensitive detector, which allows the researcher to accomplish the energy scan of the diffracted photons. In this way, the reciprocal space scan (or q -scan, $q = aE \sin \vartheta$, where q is the normalized momentum transfer magnitude, a is a constant, E is the energy of the incident X-ray beam, and 2ϑ is the scattering angle), necessary to collect the diffraction pattern, is carried out electronically, rather than mechanically, as in the conventional ADXRD method. The main advantage of the energy dispersive (ED) mode for X-ray diffraction studies is that the experimental setup is kept fixed during the pattern acquisition, which simplifies the experimental geometry and prevents systematic angular errors, as well as possible misalignments.²⁸ In particular, this technique provides faster recording of the Bragg peaks as, in the ED mode, the whole diffraction pattern is obtained in parallel at any q value. The energy resolution is about 1.5%, while the maximum count rate is around 10 kcounts/s. Source and detector arms are moved by two linear actuators driven by step motors, which guarantees a minimum scattering angle increment of 0.004°.

Fourier Transform Infrared Spectroscopy Characterization. FTIR spectroscopy analysis was carried out, collecting a sequence of spectra by means of a Jasco FT/IR 470 Plus interferometer (Italy), equipped with an IRTRON IRT-30 infrared microscope. For each sample N1–N3, a paste was prepared by mixing 0.5 g of the corresponding pristine powder with 0.5 mL of SBF, until a homogeneous cream-like paste was formed. The paste was placed on a KBr window, and the sequences of spectra were acquired in the transmittance mode in the 4000–550 cm⁻¹ range, by executing 250 scans at 8 cm⁻¹ resolution. The spectra were collected in situ from the same portion of sample starting from 5 min after its preparation and for a total of 70 h.

Scanning Electron Microscopy Characterization. SEM apparatus (TESCAN VEGA II (Czech republic)), working in secondary and backscattered electron modes, was used for morphological studies of the pristine powders and of the samples N1–N3 in SBF, 5 and 70 h after the sample preparation. The resolution of the apparatus in vacuum conditions was about 4 nm.

3. Results

Ex Situ EDXRD Measurements. For the structural characterization of the pristine powder samples N1–N3, ex situ EDXRD diffraction measurements were performed. Several diffraction patterns were collected at various scattering angles as preliminary tests, in order to find the best experimental conditions, and a wide q -scan was performed for individuating the q -region of interest. The sequence of Bragg peaks in the q -range of (1.0–4.0) Å⁻¹ was individuated, progressively increasing the scattering angle 2ϑ , at maximum beam energy corresponding to 55 keV. The most intense peaks of both OCP and DCPD fall in this q -range. Therefore, once these optimal experimental conditions were found, they were maintained for the whole set of measurements: primary beam maximum energy of 55 keV and scattering angle of $2\vartheta = 7.6^\circ$. Three samples – OCP, DCPD, and their combination – were investigated ex situ:

- sample N1: 100% OCP powder;
- sample N2: 70% OCP and 30% DCPD powder;
- sample N3: 100% DCPD powder.

In the 1.0–4.0 Å⁻¹ q -range, several peaks can be detected for all the samples (Figure 2a,b). As expected, there are similarities between the patterns corresponding to the samples N1 and N2 that share the same major component, 100% OCP and 70% OCP, respectively. After an accurate attribution of the diffracted intensities, the most intense peaks, corresponding to OCP and DCPD, are assigned in Figure 2a,b. Peaks labeled in the patterns N1 and N2 correspond to the crystalline contribution of OCP (polycrystalline, triclinic

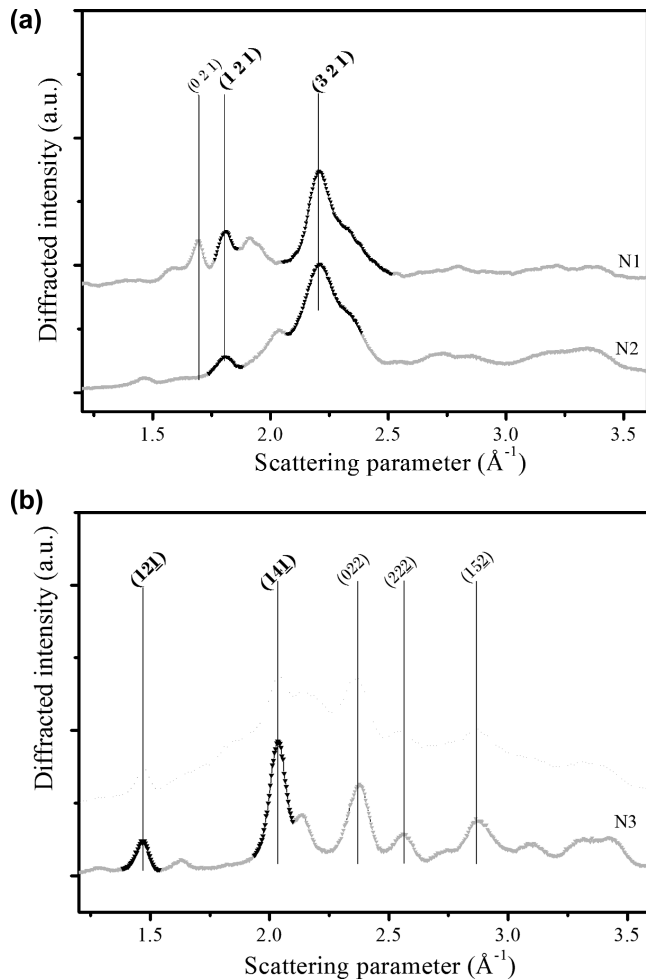


Figure 2. EDXRD patterns of the pristine powder samples: (a) N1–N2, (b) N3. The peaks chosen to study the structural behavior are marked in bold.

(card number no.: 79-0423²⁹)), while the peaks labeled in the patterns N3 correspond to the crystalline contribution of DCPD (polycrystalline, monoclinic, S.G.: Ia9 (card number 178 no. 72-0713²⁹)). For all the samples, two peaks were chosen in order to follow their structural evolution: (121) (at $q = 1.8 \text{ \AA}^{-1}$) and (321) (at $q = 2.2 \text{ \AA}^{-1}$), attributable to OCP for the sample N1–N2 group; and (12̄1) (at $q = 1.5 \text{ \AA}^{-1}$) and (14̄1) (at $q = 2.0 \text{ \AA}^{-1}$), attributable to DCPD for the sample N3. The peaks chosen for analysis are marked in bold in Figure 2a,b.

After this preliminary characterization, in situ EDXRD studies were performed under the same diffraction conditions (energy $E = 55 \text{ keV}$, scattering angle $2\vartheta = 7.6^\circ$).

In Situ EDXRD Measurements. In situ time-resolved EDXRD measurements were performed in order to follow in real time the phase transformations, occurring in the pristine powders when mixed with SBF. For each sample N1–N3, a paste was prepared by mixing 0.5 g of the corresponding pristine powder with 0.5 mL of SBF, until a homogeneous cream-like paste was formed. The paste was immediately placed in the optical center of the diffractometer, and a sequence of diffraction patterns was collected in real time. On the basis of our previous studies,^{30–32} it is possible to infer that a crystallization processes proceeds fast at the beginning and slows down upon time. For this reason, the diffraction patterns were collected every 10 min during the first hour, then every hour for the remaining 59 h. In this way, it was possible to detect the fast changes taking place at

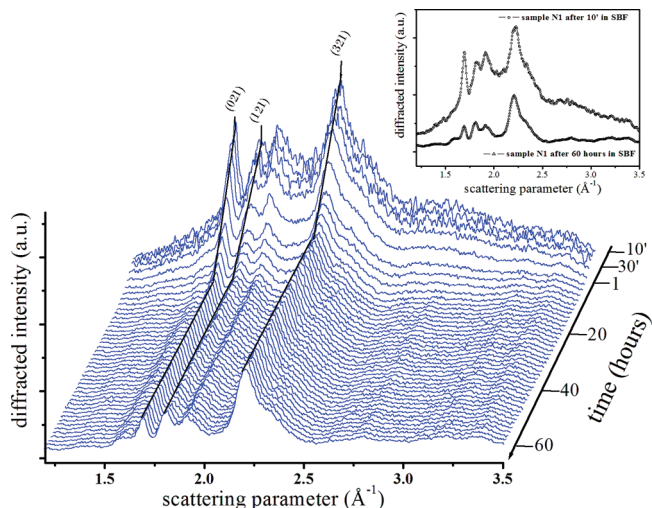


Figure 3. Sequence of diffraction patterns collected upon sample N1 in SBF for a total duration of 60 h. In the inset, the comparison between the patterns collected at $t = 10 \text{ min}$ (upper curve) and $t = 60 \text{ h}$ (lower curve) is shown.

the early stages of a transformation process. In Figure 3, a sequence of diffraction patterns, collected as a function of the scattering parameter and of time (a 3D map), is shown for the sample N1 in SBF.

At this point, some general qualitative observations can be made. In the pastes, compared to the corresponding pristine powders, the Bragg peaks are much broader and partially convolved, due to the presence of SBF liquid component. In the inset of Figure 3, a comparison between the patterns collected at $t = 10 \text{ min}$ (upper curve) and $t = 60 \text{ h}$ (lower curve) is plotted, and the structural changes taking place in the system are clearly visible: loss of the overall diffracted intensity and the shape evolution of some peaks. Similar behaviors have been previously observed by us for calcium phosphate bone cements hardening process.^{30–32} It is commonly attributed to the loss of X-ray amorphous phase contribution to the overall diffracted signal, because of the conversion of the nanophasic material into larger ordered crystallites. This loss is accompanied by an increase of some particular Bragg reflections intensity due to the formation of novel crystallites (primary crystallization), whose profile gets sharper and sharper as the new formed crystalline grains grow (secondary crystallization).

Together with this amorphous-into-crystalline conversion, another mechanism affects the Bragg reflections intensity, as can be realized looking at the inset in Figure 3. In this inset, an increase and a decrease of specific Bragg reflection relative areas, and namely the increase of the (321) peak and the decrease of the (121) and (021) peaks, is evident. Similar inverse trends have been observed in our previous study on OCP in physiological solution.³³ In that work, the loss of the (021) peak relative area was registered, whereas the (321) peak relative area increased. Indeed, the (021) peak can be associated to the OCP crystalline structure only (there is no overlap with HA reflections at $q = 1.68 \text{ \AA}^{-1}$), while the (321) reflection at $q = 2.21 \text{ \AA}^{-1}$ is the convolution of the (321) OCP peak and the (211) 100% relative intensity HA peak at $q = 2.24 \text{ \AA}^{-1}$ (hexagonal system, S.G. P6₃/m (176), card no. 74-0566²⁹). The (021) peak behavior can be considered as representative of OCP only: its relative area decreases, as was ascertained in our earlier work,³³ due to the conversion of octacalcium phosphate into HA.

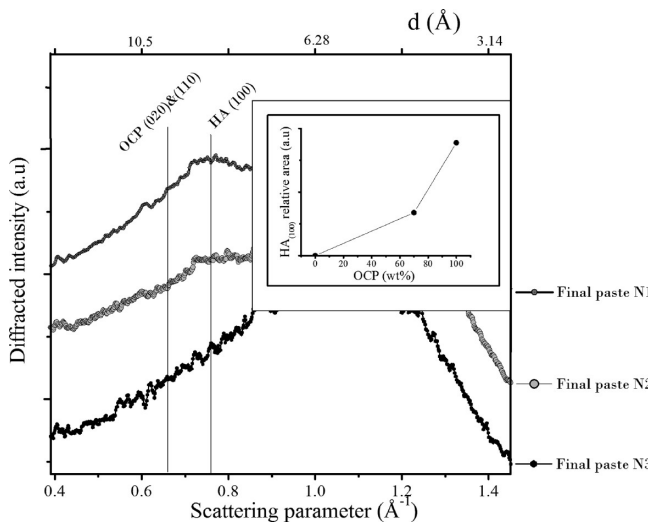


Figure 4. EDXRD patterns, collected during ex situ measurements upon the final paste N1–N3 in SBF 70 h after mixing. In the inset, relative area of the HA(100) peak is shown.

To confirm this hypothesis, that is, that the inverse peak behavior is due to the HA formation, a different q -region was explored during ex situ EDXRD measurements, analyzing the final paste. In Figure 4, the EDXRD patterns, collected 70 h after mixing upon the final pastes N1–N3 (corresponding to the samples N1–N3, respectively), is plotted. The explored q -interval ranges from 0.4 to 1.4 \AA^{-1} . This q -range was selected in order to discriminate between the OCP and HA crystalline contributions. These two compounds feature similar diffraction patterns, but the peaks detectable in the indicated q -range are separated enough to be uniquely assigned. As visible, the diffraction pattern related to the final paste N1 shows a reflection at ($q = 0.76 \text{ \AA}^{-1}$, $d = 8.16 \text{ \AA}$) corresponding to the HA (100) Bragg crystalline contribution. In the inset of Figure 4, relative area of the HA(100) peak is presented. As can be seen, it diminishes reaching zero, while passing from the final paste N1 to the paste N3.

The sequence of diffraction patterns shown in Figure 3, for the sample N1 in SBF, is a representative example of the monitoring, performed for all three samples. For each sample, a 3D map was obtained, and an accurate quantitative analysis was performed for each diffraction pattern. As was already mentioned above, for each sample two representative peaks were fit and analyzed in order to study the structural evolution of the system. In this way, information about the peak shape and its parameters, such as area, full width half maximum (FWHM), and position. Starting from these parameters and applying the diffraction theory in the proper form, that is, adapted for the energy dispersive mode, the structural data were obtained.

To calculate the crystallites average size from a diffraction pattern, the equations corresponding to the Scherrer formula (valid for the ADXRD mode only), were applied. Such equations³⁴ were obtained from the Laue formulas:

$$\frac{1}{2}tq_2 = (n+1)\pi \text{ and } \frac{1}{2}tq_1 = (n-1)\pi \quad (4)$$

where t is the crystallites average diameter; q_1 and q_2 are the interference function zeros adjacent to the function maximum ($q_1 < q_2$); n is the order of the interference function peaks (the parameter that labels the features of the “sinc”

interference function). Combining these two equations, the relation $t = 4\pi/(q_2 - q_1)$ is obtained. According to Scherrer, it can be simplified assuming a triangular shape of the interference peak, thus becoming $t \approx 2\pi/\sigma_{[hk\ell]}$, where $\sigma_{[hk\ell]}$ is the standard deviation of the $[hk\ell]$ peak intensity distribution due to the crystallite finite size. Therefore, once the contributions to the peaks broadening due to the limited instrumental resolution (i.e., to both the angular and the energy spreads) are corrected, the relation between t and $\sigma_{[hk\ell]}$ can be used to calculate the former.

Since in our systems crystallization processes take place, another parameter, such as characteristic crystallization time (τ_c), can be determined. Two alternative approaches can be applied for this purpose. The first is defining τ_c as the time corresponding to half process (when 50% of the final amount of crystallites has been formed); the second, defining τ_c as the time corresponding to the maximum transformation speed (inflection point of the growth curve). However, when crystallization follows a sigmoidal growth, these two quantities coincide. This is the case of the present study. Therefore, τ_c is determined by fitting the experimental points by a sigmoid and then, by imposing that the second derivative of the curve, is equal to zero.

In Figure 5, the time evolution of structural properties for the sample N1 in SBF, upon the 60 h process, is shown. Data processing has been performed on the (121) and (321) Bragg reflections, the (121) peak being the crystalline contribution of the octacalcium phosphate only, while the (321) Bragg reflection being the convolution of the former with the (211) HA peak. It should be stressed that the relative area of peaks was evaluated during the data processing, which means that the background baseline was properly subtracted. As can well be seen also from Figure 5, the peaks evolution proceeds in the opposite way: the (321) peak relative area increase is approximately (+60%), while the decrease in the (121) peak relative area is about (-75%). The average grain size calculated from the (121) OCP reflection does not exhibit any significant change upon the 60 h process, being about $18 \pm 1.0 \text{ nm}$. Conversely, the average grain size calculated from (321) mixed peak increases from $4.0 \pm 1.0 \text{ nm}$ to $7.0 \pm 1.0 \text{ nm}$. Indeed, when fitting the double peak as a single, the contribution to the peak broadening is mainly due to the smaller HA grains. The characteristic crystallization time of the processes calculated from the (121) OCP peak is $2.4 \pm 0.5 \text{ h}$, while that calculated from the mixed (321) peak is longer, about $3.3 \pm 0.5 \text{ h}$.

A 3D map, similar to that shown in Figure 3, was obtained also from the sample N2 in SBF. The same data analysis procedure was performed for this sample, analyzing the same Bragg reflections, for more adequate comparison. From Figure 6, it follows that, for the sample N2 in SBF, the peak relative area evolution has the same inverse trend as observed in Figure 5 for the sample N1 in SBF. For the sample N2, the (321) peak relative area increase is approximately (+38%), while the loss of the (121) peak relative area is about (-78%). The OCP grain size growth takes place, starting from $2.0 \pm 1.0 \text{ nm}$ up to $13.0 \pm 1.0 \text{ nm}$ ((121) peak analysis), while the grain size calculated from the mixed (321) peak does not show any growth, being about $6.3 \pm 1.0 \text{ nm}$. The characteristic crystallization time calculated from the (121) peak is $2.2 \pm 0.5 \text{ h}$, whereas that calculated from the mixed (321) peak is much longer, $7.2 \pm 0.5 \text{ h}$.

The formation of hydroxyapatite in this system is further confirmed by the ex situ EDXRD results presented in

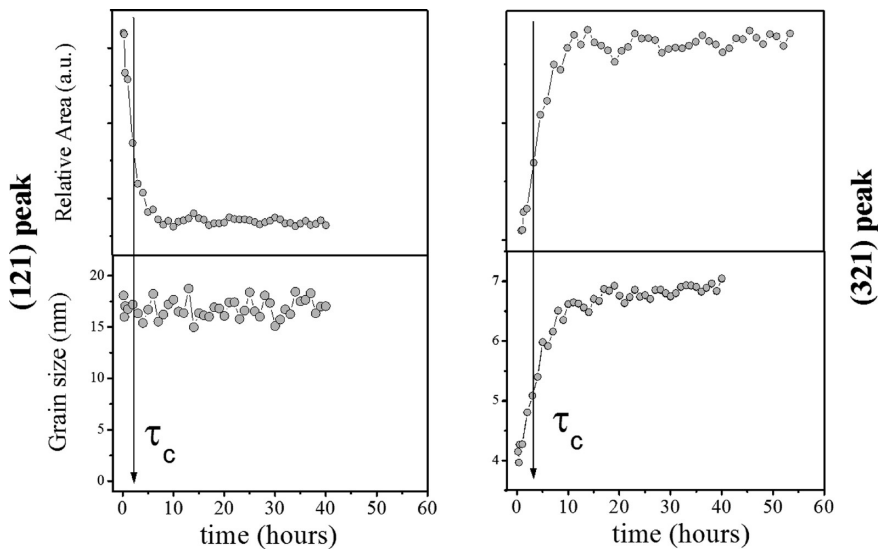


Figure 5. Time evolution of structural properties for sample N1 in SBF, related to the (121) and (321) Bragg reflections, during the 60 h process.

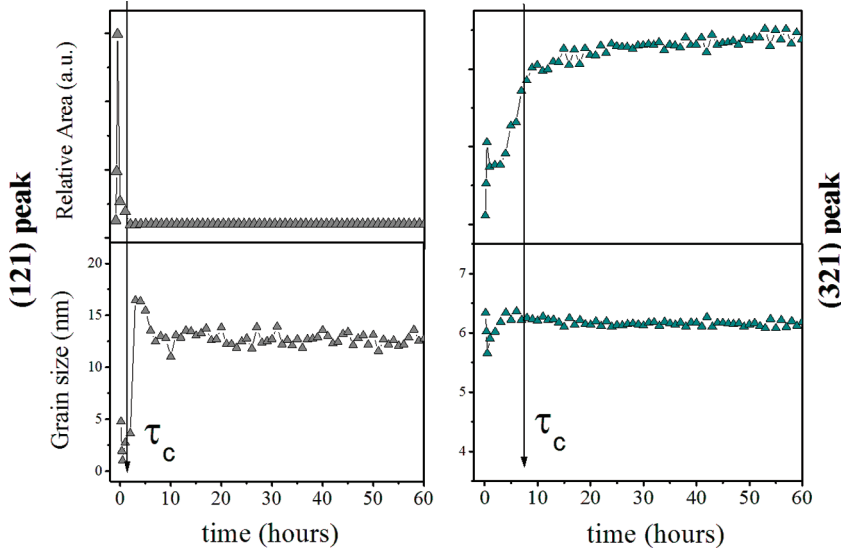


Figure 6. Time evolution of structural properties for sample N2 in SBF, related to the (121) and (321) Bragg reflections, during the 60 h process.

Figure 4 (0.4–1.4 Å⁻¹ *q*-range), where the HA (100) Bragg reflection is clearly observed in the final paste.

To follow the structural transformations of sample N3 in SBF, the $(12\bar{1})$ at $q = 1.5 \text{ \AA}^{-1}$ and $(14\bar{1})$ at $q = 2.0 \text{ \AA}^{-1}$ Bragg reflections were chosen, attributable to DCPD and marked in bold in Figure 2b. Furthermore, to check whether a transformation of DCPD into OCP or HA occurred in this system, additional Bragg reflections were followed, which were expected to increase in case of a transformation process. The (121) OCP reflection at $q = 1.8 \text{ \AA}^{-1}$ and the (321) OCP-HA mixed peak at $q = 2.2 \text{ \AA}^{-1}$ (the latter peak, as already indicated above, being the convolution with the (211) HA 100% relative intensity peak centered at $q = 2.24 \text{ \AA}^{-1}$) were followed. However, as can be seen from Figure 7, where the sequence of diffraction patterns, collected as a function of the scattering parameter and of time (3D map), is shown, for the sample N3 in SBF, there is no increase of the above indicated Bragg reflections. Therefore, no OCP and/or HA formation takes place in this system. Moreover, the ex situ EDXRD pattern of the final paste measured at low

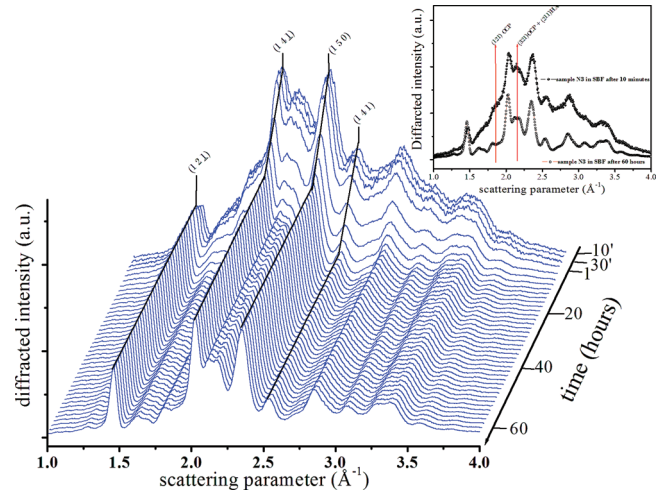


Figure 7. Sequence of diffraction patterns collected upon sample N3 in SBF for a total duration of 60 h. In the inset, the comparison between the patterns collected at $t = 10$ min (upper curve) and $t = 60$ h (lower curve) is shown.

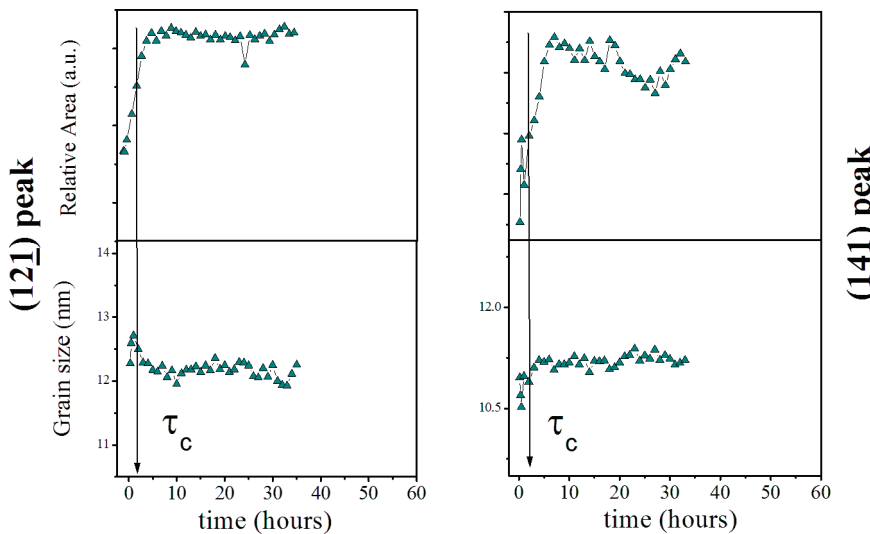


Figure 8. Time evolution of structural properties for sample N3 in SBF, related to the $(12\bar{1})$ and $(14\bar{1})$ Bragg reflections, during the 60 h process.

angle, does not contain either OCP or HA peaks (see Figure 4).

The investigation of the sample N3 (100% DCPD) in SBF has been carried out following the same data treatment procedure, as described above for the samples N1–N2. In this case, all the analyzed parameters are related to the brushite crystalline features. Figure 8 shows the time evolution of structural properties for the sample N3 in SBF, related to the $(12\bar{1})$ and $(14\bar{1})$ Bragg reflections upon 60 h of the process. For this system, both analyzed peak intensities evolution have the same trend: the $(12\bar{1})$ Bragg reflection relative area increase is about (+50%), while the $(14\bar{1})$ Bragg reflection relative area increase is approximately (+23%). The grain size versus time curve profile is almost flat (having a constant value of about 12.3 nm), when calculated from the $(12\bar{1})$ peak, while the grain size calculated from the $(14\bar{1})$ Bragg reflection shows some growth from 10.5 ± 1.0 up to 11.2 ± 1.0 nm. The characteristic crystallization time calculated from the $(12\bar{1})$ peak is 1.9 ± 0.5 h, whereas that calculated from the $(14\bar{1})$ peak is about 2.4 ± 0.5 h. Therefore, different results were obtained for the $(12\bar{1})$ and $(14\bar{1})$ Bragg reflections, belonging to different crystallographic directions of the DCPD compound.

FTIR Spectroscopy Results. To better understand the transformations taking place in the investigated systems, in situ FTIR measurements for the samples N1–N3 in SBF were carried out to study the vibrational properties of OCP, DCPA and other new molecules, if formed, in our systems. In Figure 9, a sequence of the FTIR spectra for the sample N1 in SBF, collected as a function of time, starting from 5 min after mixing and up to 70 h, is shown. On the right side of Figure 9, the $1300\text{--}550\text{ cm}^{-1}$ zone, containing the major part of absorbance bands, is presented. The spectra provide a number of details indicating that some transformations occur in this system.

A weak hydroxyl group (OH^-) stretching mode band is observed at 3750 cm^{-1} , being present in all the spectra and originated from the H_2O molecule. Another broad H_2O band is present in the $1700\text{--}1400\text{ cm}^{-1}$ range, which is not shown here, as well as the bands at 2345 and 2339 cm^{-1} , assigned to the asymmetric stretching mode of the CO_2 molecule from the air.³⁵

Phosphate bands located at 561 and 600 cm^{-1} of $\nu_4 \text{PO}_4^{3-}$ bending, 856 cm^{-1} of HPO_4^{2-} (P-OH stretching), 964 cm^{-1}

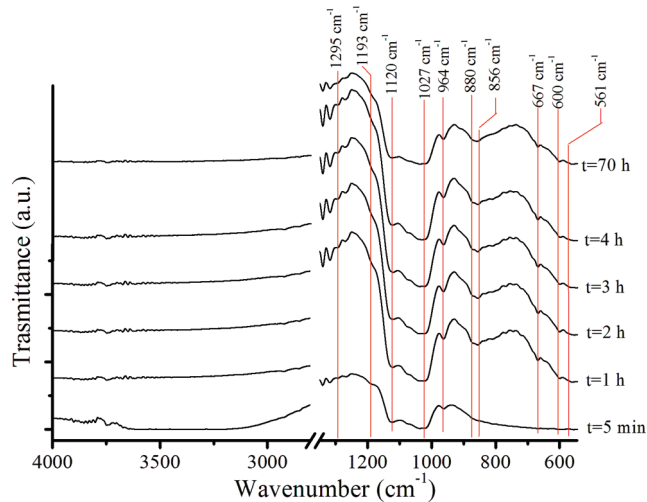


Figure 9. FTIR spectra of sample N1 in SBF (time evolution).

of $\nu_1 \text{PO}_4^{3-}$ stretching, 1027 cm^{-1} of $\nu_3 \text{PO}_4^{3-}$ stretching, 1120 cm^{-1} of $\nu_3 \text{HPO}_4^{2-}$ stretching, 1193 cm^{-1} and at 1295 cm^{-1} of HPO_4^{2-} (OH in-plane bending), and the H_2O libration at 667 cm^{-1} , were registered in our spectrum (see Figure 9). These bands could be assigned to both OCP and HA molecules.^{35–39} As one can observe, a significant change occurred in the system in the time interval from 5 min to 1 h, likely corresponding to the carbonated hydroxyapatite (CHA) formation. This hypothesis is confirmed by the appearance of an intense ν_2 carbonate vibration mode at about 880 cm^{-1} .^{35,37–42} According to the literature data, other carbonate absorbances, allowing researchers to distinguish between OCP and HA thanks to the CHA formation, $\nu_3 \text{CO}_3^{2-}$ bands, should be present in the $1300\text{--}1659\text{ cm}^{-1}$ region,⁴² or otherwise at 1450 and at 1540 cm^{-1} ,^{37,38,41} which, however, cannot be well distinguished in our spectra due to the intense H_2O absorbance in this spectral range. It should be stressed that the 880 cm^{-1} band is absent in the FTIR spectrum of the sample's N1 pristine powder. The intensities of the bands at 600 , 667 , 856 , 964 , 1027 , and 1120 cm^{-1} increased significantly upon 1 h of the process. The absence of hydroxyl stretch band at about 3570 cm^{-1} led to the opinion that the formation of completely substituted

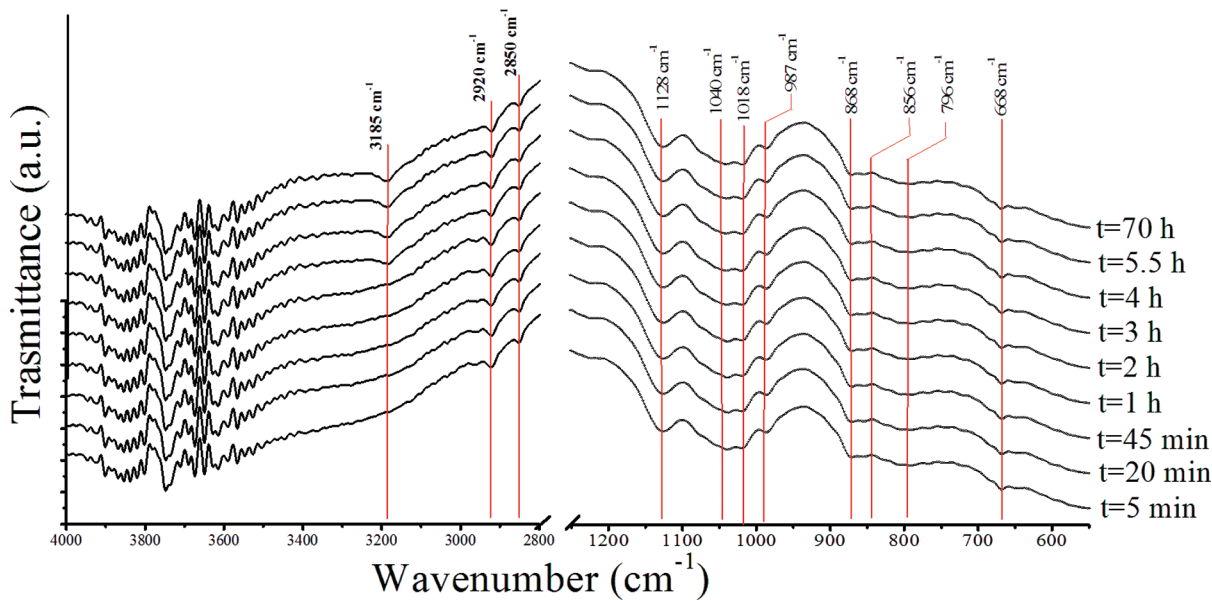


Figure 10. FTIR spectra of sample N2 in SBF (time evolution).

CHA (A-type substitution, that is, CO_3^{2-} incorporation into (OH^-) groups position in the hydroxyapatite molecule)^{35,37,38} occurred in our system.

Moreover, according to ref 36, some differences between OCP and HA can be evidenced, following the intensities evolution of some particular IR bands present in the spectra during the progressive OCP hydrolysis into HA, like the decrease of 1193 and 1295 cm^{-1} absorbances. From our spectra, a slight time decrease of the aforementioned bands can be registered by an accurate comparison of the corresponding band areas. This experimental evidence corroborates the EDXRD results, indicating that, in this system, a hydroxyapatite formation takes place.

In Figure 10, the sequence of the FTIR spectra of the sample N2 in SBF is presented. As can be noticed, in the range of 1200–550 cm^{-1} , the spectra are almost identical, while starting from the third hour, the appearance of a band at 3185 cm^{-1} can be detected in the 4000–2800 cm^{-1} range. This band can be assigned to the OH^- stretching,⁴³ which is absent in the sample's N2 powder FTIR spectrum. A more intense OH^- stretching of hydroxyapatite at about 3570 cm^{-1} cannot be well distinguished in our spectra due to the intense H_2O absorbance in the 3500–3900 cm^{-1} spectral range. This result accounts for the hydroxyapatite formation, as was clearly evidenced for this system by the EDXRD measurements.

In Figure 11, the sequence of the FTIR spectra of sample N3 (DCPD) in SBF is shown. As it is visible, all the spectra are almost identical. The literature data⁴³ for brushite vibration modes are the following: H_2O libration at 661 cm^{-1} , P–O–H out-of-plane bending at 795 cm^{-1} , P–O(H) stretching at 877 cm^{-1} , P–O and P–O–H stretching at 987 cm^{-1} , P–O stretching at 1065 and 1135 cm^{-1} . All these bands are present also in our FTIR spectra of sample N3 in SBF, and in the spectrum of DCPD powder, in good agreement with ref 43. Thus, no new molecules formation took place in this system, as evidenced also by the EDXRD measurements.

SEM Results. Morphological investigations of the systems under study were carried out utilizing the scanning electron microscopy analysis. First, the pristine powders were characterized. In Figures 12a, 13a,b, and 14a, the micrographs

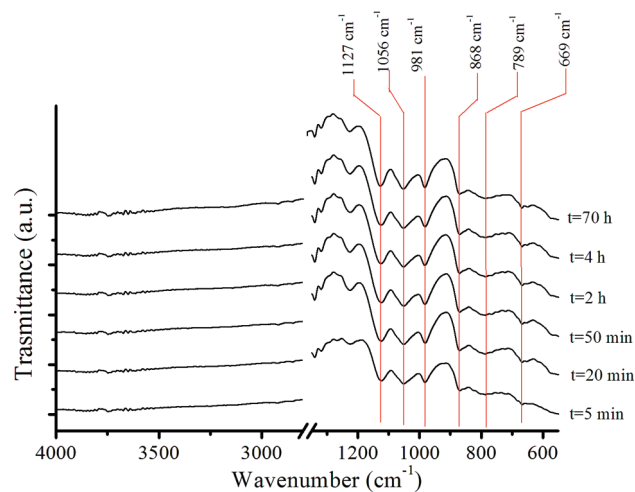


Figure 11. FTIR spectra of sample N3 in SBF (time evolution).

corresponding to the powder samples N1–N3 are presented. OCP is characterized by the plate-shaped elongated crystals of micrometer-size length (Figure 12a), whereas biphasic powder N2 (OCP–DCPD(30%)) (Figure 13a,b) has a completely different flower-shaped morphology. Agglomerates of crystals seem to grow from a central nucleus in all directions. Each flower-shaped morphology structure (Figure 13b), about 50 μm in diameter, is formed of intersecting thin petal-shaped crystals, composing a surface of flower-like structures (Figure 13a). Very similar lily-shaped morphology was reported in ref 44 for the brushite powder crystals. One can hypothesize, however, that in that work⁴⁴ a mixture of OCP–DCPD powder was obtained. Pure brushite powder crystals (sample N3) (Figure 14a) are elongated rodlike structures of several tens of micrometers in length.

From SEM images of samples N1–N3 in SBF, taken 5 h and 70 h after mixing, a change in the morphology could be detected. The original plate-shaped crystals, corresponding to the sample N1 in SBF, grew up and increased their thickness (Figure 12b,c), although 5 h (Figure 12b) and

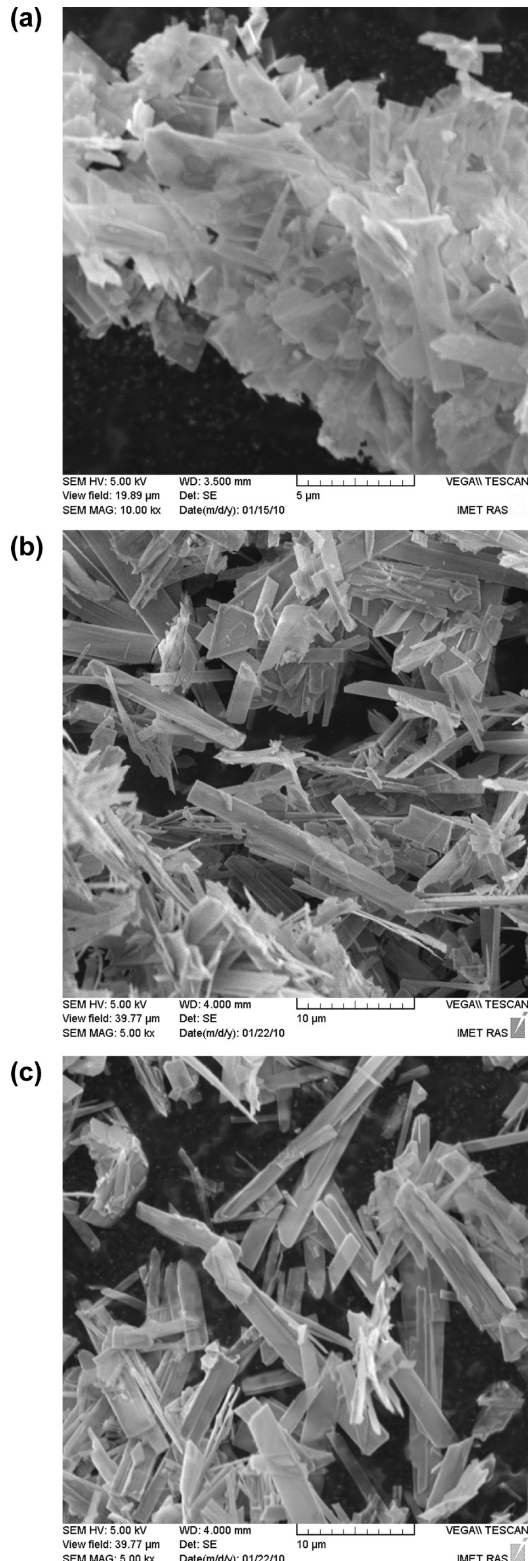


Figure 12. Sample N1: OCP powder (a); OCP + SBF 5 h (b) and 70 h (c) after mixing.

70 h (Figure 12c) morphologies do not present a significant difference. These crystals of anisotropic aspect of about 10–15 μm in length and 1.2 μm in width are very similar to the HA crystals reported in ref 45. In the case of sample N2 in SBF, flower-shaped structures dissolved completely, and two types of agglomerates appeared (long plate-shaped and small shapeless crystals) (Figure 13c). Also in this case,

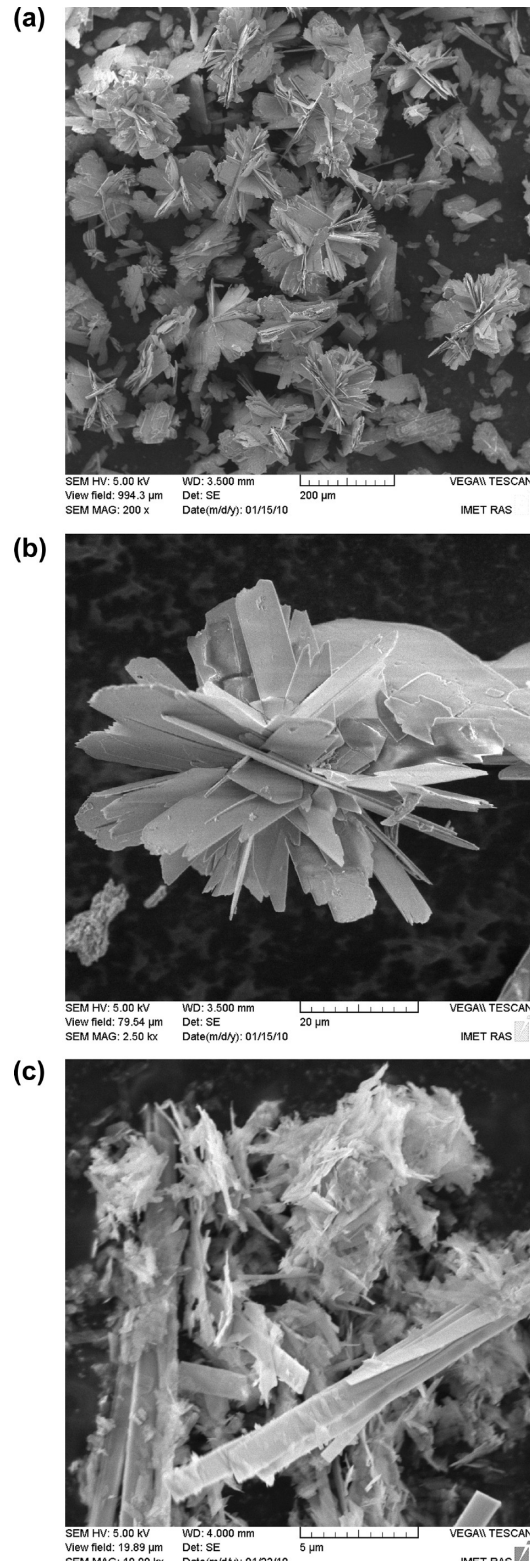


Figure 13. Sample N2: (70% OCP–30% DCPD) powder (a) and (b); (70% OCP–30% DCPD) + SBF 5 h after mixing (c).

there was no change in 5 h and 70 h morphologies. The long plate-like agglomerates are similar to the crystals, shown in Figure 12b (sample N1 in SBF after 5 h). Sample N3 (brushite) in SBF, instead, maintained its morphology (Figure 14b). It can be summarized that for all the samples, the micrographs corresponding to 5 h and 70 h morphologies showed only a very slight difference.

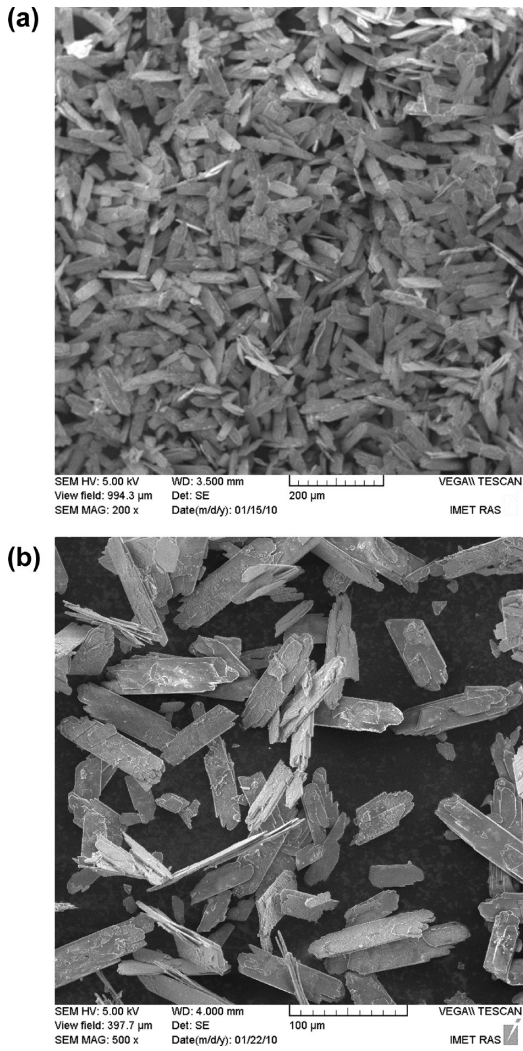


Figure 14. Sample N3: DCPD powder (a); DCPD + SBF 5 h after mixing (b).

4. Discussion

The precipitation of bioactive calcium phosphates in simulated body fluid, a solution with ion concentration and pH value similar to those of human body plasma, is of great interest because it is similar to the biological mineralization process. Numerous literature data show the transformation of OCP into HA under physiological conditions due to their mineralogical correlation, providing geometrically favorable conditions for a phase transformation.^{19,39,46,47} Implanted OCP was shown to be converted into apatite over 10 days, according to X-ray diffraction data.^{19,46,48}

In this work, the OCP–DCPD biphasic composition in SBF was investigated, in order to study the effect of secondary phase (DCPD) presence on the processes, taking place in the systems. The information gained by the joint use of the EDXRD, FTIR, and SEM techniques provided complementary and consistent results that will be discussed here, suggesting some hypotheses based on structural, chemical, and morphological considerations.

The EDXRD method supplied interesting information regarding the structural changes taking place in the systems. On the basis of the reported data, it is possible to conclude that, when 30% DCPD admixture is added to OCP (sample N2), the inhibition of the HA formation and crystallization

occurs: the (321) peak area increase is (+38%), almost two times less compared to sample N1 (+60%), the HA grain size increase is blocked at 6.3 nm, and the characteristic crystallization time is much longer (7.2 h for the sample N2 compared to 3.3 h for the sample N1).

It can be noticed that OCP has similar behavior in both systems: for the sample N2, the (121) peak relative area decrease (−78%) and the characteristic crystallization time (2.2 h) are almost the same as those for the sample N1 (−75%) and (2.4 h), respectively, the only difference being the presence of a secondary crystallization process (from 2 up to 13 nm grain size growth), in the case of sample N2.

Approximately equal time needed for the OCP transformation in the two systems and much longer time of the HA crystallization in the sample N2 - SBF system (7.2 h with respect to 3.3 h) led to the conclusion that, rather than the OCP phase transformation, the DCPD presence inhibits the process of hydroxyapatite crystallization. Thus, it might be used as an agent controlling the crystallization growth rates.

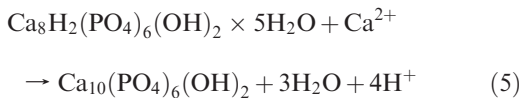
It should be noted that the similarities in the X-ray powder diffraction patterns between the HA and carbonated HA, especially in the energy dispersive X-ray diffraction mode with poor peaks resolution, did not allow us to distinguish between these two species. This is not the case for the FTIR method that allows researchers to discriminate between HA and CHA. The obtained FTIR results supply experimental evidence for the carbonated hydroxyapatite formation in the sample N1 - SBF system, and for the basic hydroxyapatite formation in the sample N2 - SBF system. The only parameter, which has no good correspondence between the results obtained by these two techniques, is the time interval. FTIR measurements report the CHA formation in the sample N1 - SBF system during the first hour after mixing, while the HA formation in the sample N2 - SBF system takes place between second and third hour after mixing, which confirms the apatite inhibition by the DCPD presence, being however, the time intervals of transformations different from those registered by EDXRD. One might suppose that the FTIR microscope mode using a halogen lamp for the measurements, leads to an increase of the system temperature, and therefore, the transformations occur faster.

The SEM results presented in this work are in good agreement with both the EDXRD and the FTIR measurements, providing further evidence for hydroxyapatite formation in the case of sample N1–N2 in SBF. According to Figure 12b,c, the 5 h and 70 h plate-shaped morphologies are developing preferentially from the former OCP phase. A similar result was obtained by the authors,³⁹ which studied the OCP hydrolysis under physiological conditions, resulting in the formation of carbonated hydroxyapatite crystals. Analogously, in this work the plate-shaped morphology of the OCP crystals remained roughly unchanged, increasing only the crystals thickness upon soaking time. Authors²¹ also confirmed that the thickening of OCP thin crystallites (in a certain crystallographic direction), thanks to their similarity to HA, provides a substrate for the HA nucleation and growth.

As it was written in the introduction section, the transformation of OCP into HA can proceed via either (1) *in situ* hydrolysis of apatitic layers (internal rearrangement process) or (2) *de novo* precipitation of apatite crystals on the OCP crystal templates, that is, the process of the OCP dissolution and the reprecipitation of apatite crystals. The results obtained in this work do not allow us to express any preferences

toward one of these hypotheses; it is likely that both the processes take place. Indeed, for the sample N1 in SBF, the second mechanism (2) is more probable: the OCP average grain size is 18 nm, likely the partial OCP dissolution occurs, but no appreciable decrease in the OCP particle size is observed, being compensated by the OCP secondary crystallization grain growth. Then, de novo precipitation, followed by the nucleation and growth of carbonated hydroxyapatite particles (from 4 up to 7 nm), occurs. For the sample N2 in SBF, the OCP grain growth from 2 up to 13 nm takes place, while the HA average grain size is constant (6.3 nm). This observation is not in disagreement with the point of view that (1) in situ hydrolysis of apatitic layers (internal rearrangement process) is responsible for the OCP/HA transformation, rather than dissolution/precipitation process.

The authors³⁹ report that the hydrolysis of the OCP into carbonated hydroxyapatite may occur by a partial dissolution of OCP due to the higher OCP solubility compared to that of HA.³⁹ Then, a reprecipitation of HA in a Ca²⁺ containing solution takes place according to the reaction 5:



The obtained SEM morphologies are not controversial to the hypothesis that, for sample N1 in SBF, the transformation of OCP into HA proceeds as (2) de novo precipitation of apatite crystals on the OCP crystal templates, namely, the process of the OCP partial dissolution and the reprecipitation of apatite crystals. Indeed, from SEM images, shown in Figure 12b,c, one can notice that OCP crystals visibly increased their thickness, compared to almost transparent crystals shown in Figure 12a. In Figure 12b,c, the 5 h and 70 h plate-shaped morphologies are developing preferentially from the former OCP phase. For the sample N2 in SBF, as one can see from Figure 13c, likely some internal rearrangement process (1) occurs. Therefore, it is possible to conclude that the DCPD addition influences the transformation mechanism.

For DCPD (sample N3) in SBF, the primary and secondary crystallization processes take place, as confirmed by the data obtained by the in situ EDXRD measurements presented in Figure 8. No new species formation, such as OCP and/or HA, occurred in this system. Furthermore, no HA peaks in the (0.4–1.4) Å⁻¹ range were observed during an ex situ EDXRD measurement on the final paste N3, as can be seen in Figure 4. One of the peculiarities of the DCPD crystallization process is the different results obtained analyzing the Bragg reflections involving different crystallographic directions. For example, the percentage of the conversion of amorphous material into the crystalline one is about 50% and 23%, as registered analyzing the (12̄1) and (14̄1) Bragg reflections, respectively. The grain size temporal curve is almost flat (about 12.3 nm), when calculated from the (12̄1) peak, while it spans from 10.5 ± 1.0 up to 11.2 ± 1.0 nm, when calculated from the (14̄1) Bragg reflection. The characteristic crystallization time calculated from the (12̄1) peak is 1.9 ± 0.5 h, whereas that calculated from the (14̄1) peak is about 2.4 ± 0.5 h. Therefore, different results obtained for the (12̄1) and (14̄1) Bragg reflections account for an anisotropic crystallization process along the different crystallographic directions of brushite. FTIR and SEM data obtained for the sample N3 in SBF

confirm that the only process taking place in this system is the DCPD crystallization, evidenced by the absence of changes in the FTIR time sequence spectra (Figure 11) and by the SEM morphologies (Figure 14).

The authors²³ analyzed the driving force and nucleation rate of a calcium phosphate precipitation in SBF based on classical crystallization theories of thermodynamics and kinetics. The thermodynamic driving forces for calcium phosphates precipitation were calculated based on the classical equation of free energy change (ΔG) in supersaturated solutions. According to the authors²³ data, the pH value is a critical factor that affects calcium phosphates precipitation. The HA precipitation is thermodynamically favorable (ΔG_{HA} becomes negative) when pH ≥ 5.4, while the OCP precipitation obtains its thermodynamic driving force when pH ≥ 6.3. The driving force for HA formation is always larger than that of OCP, although both increase with increasing pH values. Under our experimental conditions (pH ≈ 7.3–7.4), $\Delta G_{\text{HA}} \approx -8$, and $\Delta G_{\text{OCP}} \approx -4$ and, therefore, the HA formation, is thermodynamically more favorable. For brushite precipitation, there is no thermodynamic driving force ($\Delta G_{\text{DCPD}} = 0$) over the entire pH range. This might be the reason that no brushite precipitation in SBF has been previously reported in the literature, and the same results also are obtained in the present work. Nevertheless, also brushite, along with OCP and amorphous calcium phosphate, is believed to be a precursor of HA formation.¹⁹

Even in the very earlier works,²⁴ it was already mentioned that the hydrolysis of OCP in the presence of carbonate ions gives strong tests for carbonated hydroxyapatite. The formation in our systems of CHA or HA, likely can be justified by kinetic factors. Precipitation of carbonate-containing hydroxyapatite is more kinetically favorable than that of basic HA, having equal thermodynamic driving force.²³ Although the EDXRD technique does not allow one to distinguish between HA and CHA, the CHA formation is plausible from the FTIR data, showing that when only OCP is present in SBF (sample N1), it transforms into CHA, whereas cooperative OCP–DCPD interactions lead to the less kinetically favorable HA formation. Therefore, rapid transformation process leads to the CHA formation, while slower transformation tends to produce hydroxyapatite.

The last observation of this work regards the nanometer size of the apatite grain growth. The basic building blocks of teeth and bones, despite their complex hierarchical structure, are nanosized mineral particles, both during the initial formation and at later stages. The crystalline grain growth processes, monitored in this work, are in the range from a few nanometers up to approximately 20 nm. The broad peak-shapes of the HA (100) reflection (shown in Figure 4), corresponding to the final pastes N1 and N2, show the nanometer grain size of the final CHA/HA phases. The Gaussian fit allowed the calculation of the average grain size of the CHA/HA crystallites, equal to approximately 4 ± 2 nm.

5. Conclusions

This study was focused on the crystallization dynamics of biogenic calcium phosphate materials in the presence of additive molecules. Indeed, it would be of considerable biomedical value to know how such additives affect the crystallization rates, in order to control the HA crystallization in biomineratilization processes.

The complementary and consistent data were obtained by EDXRD, FTIR, and SEM techniques for three investigated

samples in SBF: (1) 100% OCP; (2) 70% OCP–30% DCPD; (3) 100% DCPD. On the basis of the reported experimental results, it is possible to conclude that pure OCP in SBF (sample N1) transforms into CHA, whereas cooperative OCP–DCPD interactions lead to the less kinetically favorable HA formation. The apatites formation occurs on different time scales for samples N1 and N2. In the case of sample N1 in SBF, the CHA characteristic crystallization time is 3.3 h, while, in the case of sample N2 in SBF, the HA characteristic crystallization time is much longer (7.2 h). The additional component (DCPD, 30 wt %) influences significantly the structural behavior of hydroxyapatite, acting as an inhibition agent of the HA crystallization. No OCP and/or HA(CHA) formation was detected for sample N3 in SBF, the only result being the DCPD crystallization process, which is anisotropic along the different crystallographic directions.

By means of the OCP–DCPD cooperation approach, the calcium phosphate based materials can be modified for implant use in bone tissue engineering. In particular, OCP based cement is of great interest for biomedical applications, and OCP can be the major phase in cement formulations. However, the OCP phase precipitates very rapidly into HA. Therefore, the observed inhibition effect of DCPD can be applied for novel self-setting calcium phosphate cement systems.

The results obtained in this work provided some insights into the biomineralization mechanism.

Acknowledgment. Financial support from the Russian Foundation for Basic Research, Grant 09-03-00187a, is deeply appreciated. V.S.K. thanks the President of the Russian Federation for financial support (Grant No. MK-2286.2009.3 for “Young Russian Scientists”). The authors thank Ph.D. student N. Bakunova for assistance in performing SEM measurements.

References

- Anselme, K.; Noël, B.; Flautre, D.; Blary, M. C.; Delecourt, C.; Descamps, M.; Hardouin, P. *Bone* **1999**, *25*, 51S–54S.
- Cancedda, R.; Dozin, B.; Giannoni, P.; Quarto, R. *Matrix Biol.* **2003**, *22*, 81–91.
- Hench, L. L.; Polak, J. M. *Science* **2002**, *295*, 1014–1017.
- Honda, Y.; Anada, T.; Kamakura, S.; Morimoto, S.; Kuriyagawa, T.; Suzuki, O. *Tissue Eng. Part A* **2009**, *15*, 1–9.
- Anada, T.; Kumagai, T.; Honda, Y.; Masuda, T.; Kamijo, R.; Kamakura, S.; Yoshihara, N.; Kuriyagawa, T.; Shimauchi, H.; Suzuki, A. *Tissue Eng.* **2008**, *14*, 965–978.
- Barrère, F.; Van Blitterswijk, C. A.; De Groot, K. *Int. J. Nanomed.* **2006**, *1*, 317–332.
- Bermudez, O.; Boltong, M. G.; Driessens, F. C. M.; Planell, J. A. *J. Mater. Sci. Mater. Med.* **1994**, *5*, 144–150.
- Bodier-Houllé, P.; Steuer, P.; Voegel, J. C.; Cuisinier, F. J. G. *Acta Crystallogr.* **1998**, *D54*, 1377–1381.
- Brown, W. E.; Eidelman, N.; Tomazic, B. *Adv. Dent. Res.* **1987**, *1* (2), 306–313.
- Johnsson, M. S.; Nancollas, G. H. *Crit. Rev. Oral Biol. Med.* **1992**, *3*, 61–82.
- Suzuki, O.; Nakamura, M.; Miyasaka, Y.; Kagayama, M.; Sakurai, M. *Tohoku J. Exp. Med.* **1991**, *164*, 37–50.
- Suzuki, O.; Nakamura, M.; Miyasaka, Y.; Kagayama, M.; Sakurai, M. *Bone Miner.* **1993**, *20*, 151–166.
- Kamakura, S.; Sasano, Y.; Homma, H.; Suzuki, O.; Kagayama, M.; Motegi, K. *J. Dent. Res.* **1999**, *78*, 1682–1687.
- Imaizumi, H.; Sakurai, M.; Kashimoto, O.; Kikawa, T.; Suzuki, O. *Calcif. Tissue Int.* **2006**, *78*, 45–54.
- Kamakura, S.; Sasano, Y.; Homma-Ohki, H.; Nakamura, M.; Suzuki, O.; Kagayama, M.; Motegi, K. *J. Electron Microsc.* **1997**, *46*, 397–403.
- Miyatake, N.; Kashimoto, K. N.; Anada, T.; Imaizumi, H.; Itoi, E.; Suzuki, O. *Biomaterials* **2009**, *30*, 1005–1014.
- Grynpas, M. D.; Omelon, S. *Bone* **2007**, *41*, 162–4.
- Jager, C.; Welzel, T.; Meyer-Zaika, W.; Epple, M. *Magn. Reson. Chem.* **2006**, *44*, 573–80.
- Suzuki, O.; Kamakura, S.; Katagiri, T. *J. Biomed. Mater. Res. B* **2006**, *77B*, 201–212.
- Brown, W. E.; Mathew, M.; Tung, M. S. *Prog. Cryst. Growth Char.* **1981**, *4*, 59–87.
- Meyer, J. L.; Eanes, E. D. *Calcif. Tissue Res.* **1978**, *25*, 209–216.
- Mann, S. *Biomineralization*; New York: Oxford University Press, 2001; pp 38–67.
- Lu, X.; Leng, Y. *Biomaterials* **2005**, *26*, 1097–1108.
- Brown, W. E.; Smith, J. P.; Lehr, J. R.; Frazier, A. W. *Nature* **1962**, *196*, 1050–1055.
- Kokubo, T.; Takadama, H. *Biomaterials* **2006**, *27*, 2907–2915.
- Kokubo, T. *Biomaterials* **1991**, *12*, 155–163.
- Kokubo, T.; Kushitani, H.; Sakka, S.; Kitsugi, T.; Yamamoto, T. *J. Biomed. Mater. Res.* **1990**, *24*, 721–734.
- Caminiti, R.; Rossi Albertini, V. *Intern. Rev. Phys. Chem.* **1999**, *18* (2), 263–299.
- International Centre for Diffraction Data, Database JCPDS, **2000**.
- Rau, J. V.; Generosi, A.; Smirnov, V. V.; Ferro, D.; Rossi Albertini, V.; Barinov, S. M. *Acta Biomater.* **2008**, *4*, 1089–94.
- Smirnov, V. V.; Rau, J. V.; Generosi, A.; Rossi Albertini, V.; Ferro, D.; Barinov, S. M. *J. Biomed. Mater. Res.: Part B – Appl. Biomater.* **2010**, *93B*, 74–83.
- Generosi, A.; Rau, J. V.; Komlev, V. S.; Rossi Albertini, V.; Fedotov, A. Yu.; Barinov, S. M. *J. Phys. Chem. B* **2010**, *114* (2), 973–979.
- Rau, J. V.; Komlev, V. S.; Generosi, A.; Fosca, M.; Rossi Albertini, V.; Barinov, S. M. *J. Cryst. Growth* **2010**, *312* (14), 2113–2116.
- Patterson, A. L. *Phys. Rev.* **1939**, *56*, 978–982.
- Rau, J. V.; Nunziante Cesaro, S.; Ferro, D.; Barinov, S. M.; Fadeeva, I. V. *J. Biomed. Mater. Res.: Part B – Appl. Biomater.* **2004**, *71B*, 441–447.
- Fowler, B. O.; Markovic, M.; Brown, W. E. *Chem. Mater.* **1993**, *5*, 1417–1423.
- Barinov, S. M.; Rau, J. V.; Nunziante Cesaro, S.; Ďurišin, J.; Fadeeva, I. V.; Ferro, D.; Medvedcký, L.; Trionfetti, G. *J. Mater. Sci.: Mater. Med.* **2006**, *17*, 597–604.
- Barinov, S. M.; Rau, J. V.; Fadeeva, I. V.; Nunziante Cesaro, S.; Ferro, D.; Trionfetti, G.; Komlev, V. S.; Bibikov, V. Yu. *Mater. Res. Bull.* **2006**, *41*, 485–494.
- Horváthová, R.; Müller, L.; Helebrant, A.; Greil, P.; Müller, F. A. *Mater. Sci. Eng., C* **2008**, *28*, 1414–1419.
- Liu, X.; Ding, C.; Wang, Z. *Biomaterials* **2001**, *22*, 2007–2012.
- Landi, E.; Celotti, G.; Logroscino, G.; Tampieri, A. *J. Eur. Ceram. Soc.* **2003**, *23*, 2931–2937.
- Rehman, I.; Bonfield, W. *J. Mater. Sci. Mater. Med.* **1997**, *8*, 1–4.
- Tortet, L.; Gavarri, J. R.; Nihoul, G.; Dianoux, A. J. *J. Solid State Chem.* **1997**, *132*, 6–16.
- Mandel, S.; Cuneyt Tas, A. *Mater. Sci. Eng. C* **2010**, *30*, 245–254.
- Tanaka, Y.; Nakamura, M.; Nagai, A.; Toyama, T.; Yamashita, K. *Mater. Sci. Eng. B* **2009**, *161*, 115–119.
- Suzuki, O.; Nakamura, M.; Miyasaka, Y.; Kagayama, M.; Sakurai, M. *Tohoku J. Exp. Med.* **1991**, *164*, 37–50.
- Suzuki, O.; Yagishita, H.; Yamazaki, M.; Aoba, T. *Cell Mater.* **1995**, *5*, 45–54.
- Suzuki, O.; Nakamura, M.; Miyasaka, Y.; Kagayama, M.; Sakurai, M. *Bone Miner.* **1993**, *20*, 151–166.